Deep-Sea Research Part II 150 (2018) 170–180

Contents lists available at ScienceDirect

Deep-Sea Research Part II

journal homepage: www.elsevier.com/locate/dsr2

Petrogenesis of alkalic seamounts on the Galápagos Platform

Darin M. Schwartz[a,*], V. Dorsey Wanless[a], Rebecca Berg[a], Meghan Jones[b], Daniel J. Fornari[b], S. Adam Soule[b], Marion L. Lytle[a], Steve Carey[c]

[a] Department of Geosciences, Boise State University, 1910 University Drive, Boise, ID 83725, United States
[b] Geology and Geophysics Department, Woods Hole Oceanographic Institution, United States
[c] Graduate School of Oceanography, University of Rhode Island, United States

ARTICLE INFO

Keywords:
Seamounts
Geochemistry
Monogenetic
Hotspot
Galápagos
Basalt
E/V *Nautilus*

ABSTRACT

In the hotspot-fed Galápagos Archipelago there are transitions between volcano morphology and composition, effective elastic thickness of the crust, and lithospheric thickness in the direction of plate motion from west to east. Through sampling on the island scale it is unclear whether these transitions are gradational or sharp and whether they result in a gradational or a sharp boundary in terms of the composition of erupted lavas. Clusters of interisland seamounts are prevalent on the Galápagos Platform, and occur in the transition zone in morphology between western and eastern volcanoes providing an opportunity to evaluate sharpness of the compositional boundary resulting from these physical transitions. Two of these seamounts, located east of Isabela Island and southwest of the island of Santiago, were sampled by remotely operated vehicle in 2015 during a telepresence-supported E/V *Nautilus* cruise, operated by the Ocean Exploration Trust. We compare the chemistries of these seamount lavas with samples erupted subaerially on the islands of Isabela and Santiago, to test whether seamounts are formed from melt generation and storage similar to that of the western or eastern volcanoes, or transitional between the two systems. There are no systematic variations between the two seamounts and variability in all samples can be related through < 10% fractional crystallization at 500–900 MPa. Both seamounts are interpreted to represent a single magmatic episode and eruptive event. Trace element compositions indicate they formed downstream of the hotspot center. The calculated extents of melting are consistent with generation of magmas sourcing the seamounts beneath lithosphere of intermediate thickness (~ 56 km). The seamount lavas have compositions that are nearly identical to a subset of lavas erupted subaerially on Santiago Island, suggesting lateral magma transport on the order of 10 km from their source region prior to eruption. The compositional characteristics and, in particular, depth of crystallization suggest that although seamount magmas have a transitional melting signature, they are discretized on the island scale, through homogenization in the lithospheric mantle and redistributed by vertical and horizontal diking in the shallow crust. Due to this homogenization, it remains unclear whether the variation in erupted lava chemistries from west to east are representative of sharp or gradual changes in mantle composition and structure across the archipelago.

1. Introduction

The lifespan of hotspot sourced volcanic islands is controlled by the interplay between volcano growth (i.e., eruption rate), subsidence and erosion (e.g., Geist, 1996; Geist et al., 2014a). These processes are modulated by the transport of the islands away from a fixed "plume" source by plate motion (e.g., Morgan, 1972). The archetypal example of this process is the Hawaiian Island chain. The Hawaiian Islands form a linear, age-progressive, volcanic succession parallel to the direction of absolute plate motion, where large, young islands become progressively smaller, older and more dissected to the northwest (e.g., Clague and Dalrymple, 1987). This general progression is less clear for other plume-sourced intraplate volcanic systems, including the Galápagos Archipelago, which is the subject of this study (Fig. 1).

The Galápagos consists of 13 major volcanic islands and numerous smaller islands, and volcanic seamounts in the eastern equatorial Pacific (Fig. 1; McBirney and Williams, 1969; Christie et al., 1992). Most of the islands rise from a large (~ 3500 km^2), shallow volcanic platform that stands ~ 3000 m above the surrounding seafloor (Geist et al., 2008a). The center of plume upwelling in the Galápagos lies southwest of Fernandina Island, the westernmost and most active volcano (Allan and Simkin, 2000). The position of the plume source has been inferred based on a locally thin mantle transition zone (Fig. 1; Hooft et al., 2003), low shear-wave velocities (Villagómez et al., 2007,

* Corresponding author.
E-mail address: darinschwartz@boisestate.edu (D.M. Schwartz).

http://dx.doi.org/10.1016/j.dsr2.2017.09.019

Available online 05 October 2017
0967-0645/ © 2017 Elsevier Ltd. All rights reserved.

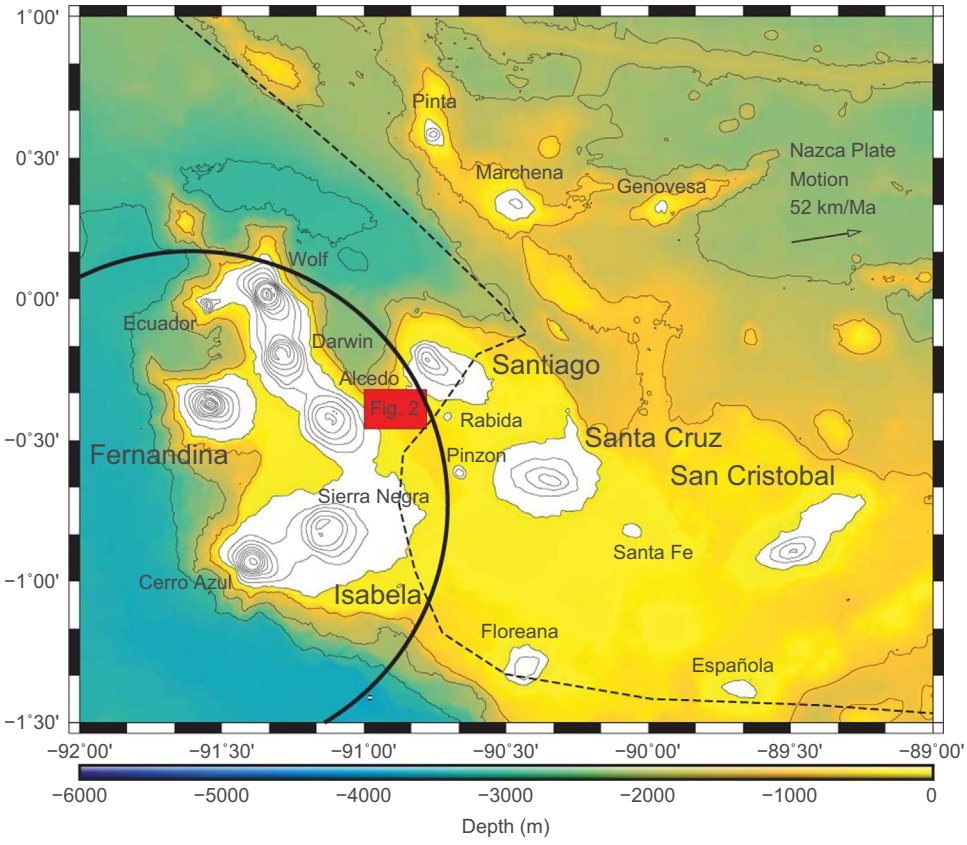

Fig. 1. Map of the Galápagos Archipelago. The western islands (Isabela, Fernandina) are typified by steep upper flanks and central calderas, eastern islands (Santiago, Santa Cruz, San Cristobal) have shallow slopes and are characterized by dispersed linear volcanic vent systems. Subaerial contours show elevations at 200 m intervals. Submarine contours show bathymetry at 500 m intervals. Solid black circle indicates boundary of anomalously thin mantle transition zone, inferred as plume upwelling region centered below Fernandina (Hooft et al., 2003). Dashed line shows boundary between high (12 km to the west) and low (6 km to the east) effective elastic thickness of the crust (Feighner and Richards, 1994), which correlates with the boundary of thick and thin mantle lithosphere (Villagómez et al., 2007). Location of seamounts sampled in this study is shown by the red region, and in more detail in Fig. 2. (For interpretation of the references to color in this figure legend, the reader is referred to the web version of this article).

2011), and geochemical enrichment (e.g., Kurz and Geist, 1999). Although there is a general age progression akin to that of Hawaii (White et al., 1993), the Galápagos differs from Hawaii in the persistence of volcanic activity up to 250 km away from the inferred plume center (e.g., Geist et al., 1986), and a wide distribution of islands and seamounts towards the Galapagos Spreading Center, attributed to plume ridge interaction (Harpp and Geist, 2002; Harpp et al., 2003). Despite continued volcanism away from the locus of mantle upwelling, there are clear differences in the magmatic plumbing systems between the western and eastern volcanoes in the Galápagos.

The Galápagos Archipelago displays a unique, systematic variation in morphology between the volcanoes in the west compared to those in the east. The western islands (Fernandina and Isabela; Fig. 1) are typified by the presence of large and multicyclic summit calderas, surrounded by circumferential fissures near the summits and radial vents on the flanks (Chadwick and Howard, 1991), which are indicators of the presence of persistent shallow (~ 2 km; Yun et al., 2006; Geist et al., 2008b, 2014b) magma chambers and periodic eruption cycles (Chadwick and Dieterich, 1995). The western volcanoes typically erupt homogenous tholeiitic lavas, resulting from primarily shallow (200 MPa; Geist et al., 1998) crystal fractionation (< 7% MgO; e.g., Saal et al., 2007). By contrast, older islands to the east (Santiago, Santa Cruz, San Cristobal, Floreana, and satellite islands; Fig. 1) are broad shields that generally lack calderas, and are dominated by flank eruptions, spatter or cinder cones, and elongate rift zones that extend from the island summit to the lower subaerial flanks (e.g., Swanson et al., 1974; Geist and Harpp, 2009). The lavas erupted on the eastern islands and in the central archipelago (e.g., Santiago; Santa Cruz) are highly variable in composition, with rock types ranging from picrites to trachytes (McBirney and Williams, 1969; Swanson et al., 1974; Saal et al., 2007; Herbert et al., 2009; Gibson et al., 2012; Wilson, 2013) and have signatures of deep crystal fractionation (600–900 MPa; Geist et al., 1998).

This transition between western and eastern volcano morphology is mirrored by a transition in both the effective elastic thickness of the crust from 12 km in the west to 6 km in the east (Feighner and Richards, 1994) and lithospheric thickness from 70 km in the west to 40 km in the east (Villagómez et al., 2007). The change in lithospheric thickness ultimately affects the total extent of mantle melting and therefore magma compositions produced in each region (Fig. 1; Gibson and Geist, 2010). However, because sampling has been restricted primarily to the subaerial islands, it is unclear whether the crustal and lithospheric thickness variations and resulting geochemical signals are abrupt or gradational across the archipelago.

In 2015, we explored and sampled two seamounts that lie between Isabela in the west and Santiago, which presently erupt as caldera-forming and dispersed styles. The seamounts are within the transition between thin and thick lithosphere (e.g., Villagómez et al., 2007) to determine if there are systematic changes in lava compositions that correlate with geophysical transitions. Specifically, the seamounts are located between Isabela in the west and Santiago in the eastern region of the archipelago (Fig. 1). We present the first suite of geochemical data from these seamounts with twelve samples collected by the remotely operated vehicle (ROV) *Hercules*. Analyses of these samples (major and trace element concentrations and volatile contents) provide the first direct measurements of interisland volcanic activity in the modern archipelago. We use these samples to 1) determine depths of crystallization and compositional heterogeneity beneath the seamounts, 2) compare the chemical characteristics of the seamounts to those of the adjacent western and eastern volcanic islands, and 3) test whether the seamounts are formed through magma delivery from a distinct deep magmatic source directly below the seamounts, or from a magma reservoir that also feeds an adjacent volcanic island.

2. Remotely operated vehicle (ROV) dives and sample collection

Rock samples were collected in collaboration with the Ocean Exploration Trust on the *E/V Nautilus* cruise NA064 in July 2015 using

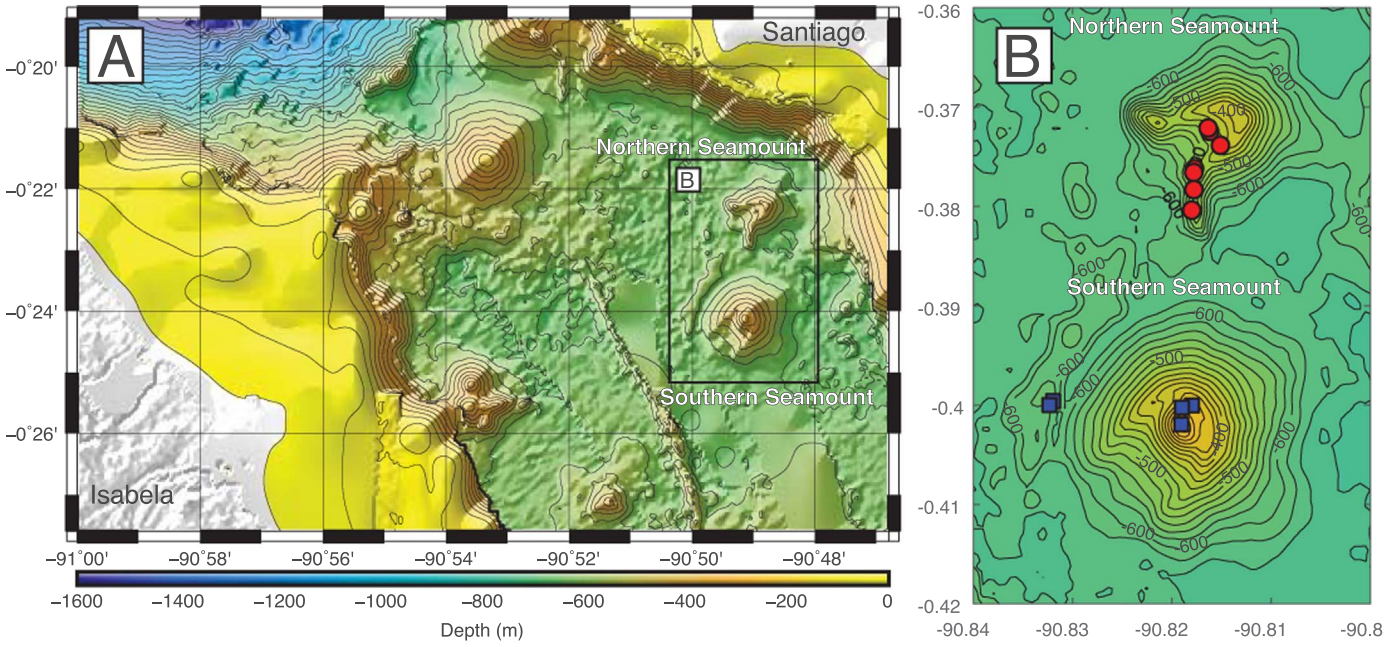

Fig. 2. A) Bathymetric map of the northern and southern seamount region The seamounts are in the central Galápagos and are on top of the Galápagos platform with basal depths ~ 600 m. Contour interval is 50 m. The nearest islands are Santiago, 5 km to the northeast, and Isabela, 10 km to the west. Black box shows location of inset map. **B) Inset Map of Seamounts** Colored symbols show sample locations. Colormap is the same as in A, contour interval is 20 m. (For interpretation of the references to color in this figure legend, the reader is referred to the web version of this article).

Table 1
Sample names and locations.

Sample locations			
Sample	**Long**	**Lat**	**Elev (m)**
Northern Seamount			
NA064-114	−90.81503	−0.37395	−422
NA064-115	−90.81612	−0.37255	−439
NA064-116	−90.81627	−0.37220	−420
NA064-120	−90.81763	−0.37630	−450
NA064-123	−90.81772	−0.37668	−445
NA064-127	−90.81770	−0.37840	−469
Southern Seamount			
NA064-129	−90.81792	−0.38047	−472
NA064-131	−90.81907	−0.40192	−265
NA064-132	−90.81797	−0.40003	−329
NA064-133	−90.81900	−0.40025	−325
NA064-134	−90.83197	−0.39960	−588
NA064-135	−90.83233	−0.39998	−587

the ROV *Hercules* (Bell et al., 2016). Dive planning and sample collection was coordinated via telepresence from the Woods Hole Oceanographic Institution's Exploration Command Center. Instructions to the onboard team of engineers and scientists were provided via satellite link using both voice, text-based chat, and video links, with real-time data transmitted from the ROV. The dive traversed two unnamed seamounts southwest of Santiago (Fig. 2) and collected 15 rock samples (seven analyzed from the northern seamount and five analyzed from the southern seamount; Table 1), in addition to extensive high definition video footage and digital still imagery (Carey et al., 2016). While nearby seamounts observable in the existing Galápagos multibeam bathymetry are nearly conical in shape (Fig. 2), both seamounts explored during this cruise are more complex, consisting of a central dome of pillow lavas flanked by a semicircular ring of volcaniclastic sediment and talus.

2.1. Northern seamount description

The northern seamount has a diameter of 1.6 km is 263 m tall, and has a volume of 0.14 km^3 (Fig. 2). The base of the seamount lies at 645 m depth and the shallowest point on the eastern summit is at 381 m depth. The summit consists of a horseshoe shaped crater rim, open to the west, composed predominately of volcaniclastic sediment, with a small summit depression containing a lava dome or flow in its center. A N-S linear volcanic ridge extends south from the seamount.

The outer slopes of the seamount are comprised predominately of unconsolidated, tan sediment at the base of the seamount with increasing proportions of, volcaniclastic, black sediment towards the top. The seamount has upper flank slopes that average 23°, with sparse cobbles or boulders of volcanic rock that increase in size with shallower depths. No in situ lava flows were observed or sampled on the volcano flanks, but two loose rocks, heavily coated with biological material, were collected from the upper third of the exterior (NA064-113) and interior (NA064-114) slopes. Within the summit depression a small dome or lava flow stands ~ 20 m above the surrounding seafloor. The dome flow is composed almost entirely of basaltic lava, lightly dusted with sediment. The morphology of the flow ranges from intact and broken pillows to hackly or jumbled lava. Two in situ samples were collected from this outcrop (NA064-115 and 116).

The linear volcanic ridge extending south of the crater is ~ 0.5 km long and consists of three small mounds (decreasing in elevation to the south). The tops of the three mounds are composed of relatively large intact pillow lavas, while the lower slopes consist of lavas and sediment. The linear ridges connecting the mounds are composed of smaller pillow tubes with minor volcanic sediment. Lava samples NA064-120 and NA064-123 were collected from the first mound and samples NA064-127 and NA064-129 were collected from the top of the two smaller mounds to the south (Fig. 2).

2.2. Southern seamount description

The larger southern seamount has diameter of ~ 3 km, a height of 388 m, and a volume of 0.34 km^3 (Fig. 2). The base of the seamount lies

at 653 m depth and the shallowest point is at 265 m depth. The summit is located at the center of the seamount and is composed of spatter and pillow lavas. Upper flank slopes average ~ 18° and are composed of unconsolidated sediment and a few sparse cobbles. The semi-circular flank is open to the southwest.

The slopes and crater rim of the seamount are composed almost entirely of tan sediment, with very sparse boulders of volcanic rock. One loose sample was collected from the northern rim of this seamount (NA064-132). The central peak is composed of loose pebble- to cobble-sized basaltic material, which bears resemblance to subaerial spatter (Sample NA064-131). The only intact lava observed on this seamount is a pillow and hackly lava flow that originates near the peak of the central dome and flows downslope to the north. One sample of this lava flow was collected (NA064-133). Two samples (NA064-134 and 135) were collected from heavily sedimented seafloor west of the seamount.

3. Geochemical methods

Samples were crushed using a mechanical jaw crusher at Boise State University. Crushed rock chips were rinsed in an ultrasonic bath using a 1% hydrogen peroxide solution, followed by DI water until clean. Approximately 1–2 mm-sized cleaned chips were handpicked using a binocular microscope, avoiding phenocrysts and alteration. Oxidized surfaces were unavoidable on two heavily altered samples (115 and 120).

Whole rock major and select trace element contents were analyzed using a Thermo-ARL automated X-ray Fluorescence (XRF) spectrometer at Washington State University (Table 2). Clean chips (25–50 g) were powdered using a ring mill with tungsten carbide surfaces and fused with Li-tetraborate into glass beads for analyses, following methods of Johnson et al. (1999). Sample NA064-115 was run with a repeat bead to assess procedural reproducibility, which is ≤ 1% difference for all elements; these two analyses were averaged.

Whole rock trace element contents were analyzed by solution ICP-MS at Boise State University following the procedures of Kelley et al. (2003) and Lytle et al. (2012) (Table 3). Approximately 50 mg of each sample were digested in closed 23 mL Savillex Teflon beakers in 3 mL of 8 N HNO_3 and 1 mL of HF. Sealed capsules containing sample-acid solution were placed on a hot plate at ≤ 100 °C overnight (~ 12 h) until no trace of solids remained. Dissolved samples were then evaporated to dryness, uncapped on a hot plate, keeping surface temperature ≤ 100 °C, and then re-dissolved in 3 mL of 8 N HNO_3 and 3 mL of ultra-pure de-ionized H_2O in sealed capsules on a hot plate at ≤ 100 °C for ~ 12 h. The dissolved samples were transferred into 125 mL HDPE bottles for a 2500× ultra-pure water dilution and sonicated for 30 min to ensure dissolution of all precipitates. Trace element concentrations were measured using a Thermo Electron X-Series II Quadrupole Inductively Coupled Plasma Mass Spectrometer (ICP-MS) coupled with an ESI SC-*FAST* autosampler. Samples were corrected using an internal standard solution containing In, blank corrected using a procedural blank, drift corrected using Geological Survey of Japan (GSJ) standard JB-3, dilution weight corrected, calibrated using US Geological Survey (USGS) standards, GSJ standards, and internal laboratory standards: BHVO-2, BIR-1, DNC-1, W-2 (USGS), JB-3 (GSJ), and 2392-9

Table 2
XRF derived major and trace element concentrations for seamount lavas, and SIMS derived volatile concentrations for sample NA064-114. Analytical precision is reported in Johnson et al. (1999).

XRF derived major/trace element concentrations and SIMS derived volatile element concentrations													
NA064-	**114**	**115**		**116**	**120**	**123**	**127**	**129**	**131**	**132**	**133**	**134**	**135**
Major element concentrations (wt%)													
SiO2	44.64	44.44	44.26	46.72	46.24	46.54	45.27	46.61	46.48	46.33	45.07	46.65	46.80
TiO2	2.238	2.178	2.167	2.248	2.324	2.380	2.386	2.318	2.253	2.368	2.372	2.438	2.342
Al2O3	15.31	15.18	15.16	16.07	15.76	15.89	15.68	16.03	15.56	15.76	15.80	15.73	15.71
FeO*	11.52	14.42	14.27	11.69	12.06	12.45	12.85	12.21	11.35	11.51	11.69	11.81	11.66
MnO	0.175	0.190	0.188	0.191	0.209	0.185	0.190	0.212	0.176	0.177	0.161	0.185	0.180
MgO	8.64	8.36	8.34	8.10	8.88	8.17	8.36	8.99	9.42	8.87	7.74	8.77	8.70
CaO	11.95	9.10	9.06	10.81	10.20	10.34	10.10	10.08	10.59	10.53	11.49	10.23	10.35
Na2O	2.78	2.52	2.52	2.85	2.88	2.90	2.82	2.84	2.75	2.93	2.66	2.96	2.85
K2O	0.39	0.61	0.61	0.37	0.38	0.42	0.42	0.39	0.36	0.34	0.40	0.38	0.46
P2O5	0.257	0.489	0.485	0.277	0.283	0.282	0.326	0.266	0.247	0.254	0.775	0.258	0.258
Sum	97.90	97.48	97.06	99.32	99.21	99.56	98.40	99.95	99.18	99.07	98.16	99.41	99.30
LOI %	1.74	2.16	2.16	0.00	0.00	0.00	0.76	0.00	0.00	0.00	1.38	0.00	0.00
Trace element concentrations (ppm)													
Ni	173	176	178	142	178	158	163	179	192	168	182	163	162
Cr	239	282	282	244	246	229	247	247	334	284	358	231	276
Sc	27	28	27	31	30	29	27	29	30	30	31	28	29
V	250	249	245	277	268	283	267	265	275	279	282	278	275
Ba	66	65	70	65	72	72	72	75	68	70	62	74	68
Rb	7	11	10	5	7	7	7	7	6	5	8	7	8
Sr	717	352	350	311	319	315	387	313	318	327	400	335	323
Zr	147	144	143	148	151	155	157	152	146	152	148	154	154
Y	27	27	26	28	28	30	29	28	27	27	31	28	27
Nb	12.5	11.1	11.4	12.3	12.5	13.3	12.4	13.0	12.1	13.3	12.9	13.6	12.3
Ga	19	17	16	20	19	19	19	20	19	19	18	20	20
Cu	61	55	57	71	61	54	60	59	68	67	51	66	66
Zn	97	108	114	101	108	108	110	114	104	184	175	134	114
Pb	1	1	1	2	1	1	2	1	1	1	3	1	1
La	12	9	10	11	9	13	16	15	12	10	14	12	12
Ce	29	25	24	30	29	30	30	27	25	32	26	33	28
Th	2	2	1	1	1	1	2	1	0	1	2	2	1
Nd	18	16	17	20	20	19	18	19	19	20	20	20	19
U	2	9	7	1	2	2	2	1	1	2	4	1	3
Volatile element concentrations (ppm)													
NA064-	**H2O**	**CO2**	**S**	**Cl**	**F**								
114	8700	135	1636	210	891								

Table 3
ICPMS derived trace element contents for seamount lavas; all concentrations are reported in ppm. Analytical precision is reported in the Supplementary data tables.

ICPMS derived trace element concentrations												
NA-064-	**114**	**115**	**116**	**120**	**123**	**127**	**129**	**131**	**132**	**133**	**134**	**135**
Li	6.11	5.51	5.39	5.57	5.83	6.06	5.48	6.67	6.28	5.54	5.89	5.15
Sc	27.9	27.8	31.5	27.6	29.1	28.0	26.7	32.1	29.0	29.9	26.3	28.7
V	240	238	264	243	253	244	232	278	255	256	239	245
Cr	235	184	184	201	184	196	188	270	220	287	218	219
Co	57.6	48.2	48.3	56.6	49.5	51.3	56.8	48.1	52.5	51.3	51.0	52.0
Ni	200	139	113	189	126	149	217	124	165	196	153	167
Cu	76.6	63.8	73.2	78.6	59.8	62.5	57.9	83.9	72.5	65.8	62.0	64.5
Zn	117.0	120.3	123.2	110.8	112.6	114.0	110.0	114.8	295.1	114.6	110.9	107.4
Ga	12.9	12.5	13.4	12.6	13.4	13.0	12.7	13.3	13.3	12.8	13.5	12.9
Rb	6.53	6.03	6.32	6.03	6.52	6.42	6.06	6.25	5.49	8.20	5.23	6.76
Sr	312	296	306	301	317	308	303	337	319	342	344	314
Y	27.4	26.1	29.1	27.1	28.5	27.8	26.2	29.5	27.8	28.1	26.3	26.6
Zr	167	147	151	146	155	156	145	170	159	155	150	151
Nb	14.3	12.6	13.8	13.8	14.4	14.1	13.4	14.7	14.7	13.7	14.5	14.2
Cs	0.06	0.07	0.06	0.06	0.07	0.06	0.06	0.06	0.05	0.22	0.05	0.07
Ba	60.2	56.5	60.2	60.1	63.1	63.3	58.8	63.9	65.0	56.3	64.0	60.9
La	10.5	9.4	10.3	10.2	10.6	10.5	9.9	11.0	10.9	10.2	11.0	10.5
Ce	27.1	24.4	26.8	26.4	27.6	27.4	25.1	28.2	27.9	26.3	27.9	26.7
Pr	3.94	3.58	3.93	3.86	4.07	3.96	3.69	4.19	4.15	3.93	4.11	3.85
Nd	17.8	16.2	17.9	17.5	18.5	18.1	16.8	19.3	18.9	17.9	18.7	18.2
Sm	4.65	4.34	4.77	4.63	4.87	4.78	4.46	5.06	4.83	4.65	4.86	4.68
Eu	1.62	1.50	1.65	1.58	1.66	1.65	1.54	1.74	1.72	1.63	1.67	1.62
Gd	5.33	4.98	5.54	5.29	5.64	5.55	5.11	5.74	5.56	5.38	5.44	5.28
Tb	0.92	0.85	0.94	0.90	0.96	0.92	0.87	0.97	0.92	0.91	0.90	0.89
Dy	5.19	4.84	5.37	5.10	5.29	5.26	4.76	5.54	5.10	5.13	5.02	4.97
Ho	0.99	0.95	1.05	0.98	1.01	1.02	0.94	1.08	1.01	1.02	0.98	0.99
Er	2.60	2.52	2.79	2.53	2.69	2.65	2.45	2.82	2.65	2.64	2.52	2.53
Tm	0.38	0.37	0.42	0.38	0.40	0.39	0.36	0.42	0.39	0.39	0.36	0.37
Yb	2.28	2.17	2.45	2.23	2.31	2.32	2.13	2.44	2.25	2.31	2.16	2.15
Lu	0.34	0.32	0.37	0.33	0.34	0.34	0.32	0.36	0.33	0.34	0.31	0.32
Hf	3.91	3.63	3.99	3.86	4.04	4.01	3.73	4.11	4.05	3.91	3.95	3.91
Ta	1.04	0.84	0.92	0.92	0.96	0.96	0.87	0.94	0.96	0.91	0.97	0.93
Pb	1.87	0.86	0.97	1.06	1.21	0.78	0.71	2.63	1.17	1.09	1.22	0.91
Th	0.89	0.76	0.83	0.84	0.88	0.86	0.80	0.86	0.87	0.80	0.92	0.84
U	0.31	0.61	0.47	0.71	0.80	0.32	0.33	0.33	0.29	1.74	0.28	0.57

(University of Florida in-house standard; Goss et al., 2010). Trace element concentrations for each sample are reported as the mean of three individual analyses, the precision is reported as the standard deviation of these analyses (Supplementary data tables).

Only one sample had glass suitable for volatile analyses. Volatile contents were measured on a glass chip from sample NA064-114 using the Cameca 1280 Secondary Ion Mass Spectrometer at Northeast National Ion Microprobe Facility (NENIMF) at the Woods Hole Oceanographic Institution, using a Cs^+ beam with a 30 μm raster size, field aperture of 1250 μm and entry slit of 81 μm, following methods by Hauri et al. (2002, Table 2). The glass fragment was hand-polished using a range of grits on silica carbide sandpaper, mounted in indium, and polished at 6, 3, and 1 μm diamond polish and 1 μm alumina grit for 5–30 min each. Volatile standard 519-4-1 (Hauri et al., 2002) was measured routinely throughout the session to monitor for instrumental drift. Measurements were calibrated with a known set of standard glasses provided by the NENIMF.

4. Results

Samples from both seamounts have vesicularities on the order of 50%. All samples contain 1–3%, ~ 1 mm plagioclase and olivine phenocrysts, with the exception of sample 131, which has ~ 7% olivine phenocrysts that are up to 2 mm. Major element contents are reported in Table 2. All of the samples are relatively mafic basalts, with MgO contents ranging from 7.74 to 9.42 wt% (Fig. 3). The degree of alteration observed in hand samples correlates with high loss on ignition (LOI; Table 2). Samples with LOI > 1% greatly increase the variability of major elements including FeO_T, P_2O_5, CaO and Na_2O (Fig. 3). Excluding sample 115, which is the most pervasively altered (2.38 wt% LOI), most of the major elements have relatively limited variability, with Al_2O_3 ranging from 15.31 to 16.07 wt%, TiO_2 from 2.18 to 2.44 wt %, Na_2O from 2.52 to 2.96 wt%, and K_2O from 0.34 to 0.46 (Fig. 3). There is slightly higher variability in CaO (9.10–11.95 wt%) and FeO_T (11.35–12.85 wt%). CaO/Al_2O_3 ratios range from 0.60 to 0.78 (Fig. 4). The basalts are all mildly alkalic, with total alkali contents (Na_2O + K_2O) ranging from 3.06 to 3.35 and SiO_2 contents of 44.64–46.80 wt% (Fig. 3).

Trace element contents are reported in Table 3, uncertainties are reported in the Supplementary data tables. Samples from both seamounts span a narrow range in incompatible trace element concentrations (e.g., 13–15 ppm Nb, 56–65 ppm Ba; Fig. 5). Despite the slight variations in concentration, the samples have low variability in CI chondrite normalized (McDonough and Sun, 1995) trace element ratios (e.g., $[La/Nb]_N$ 0.74–0.77; Fig. 6). REE patterns are nearly uniform for all samples, with a negative slope at increasing atomic mass and slight concave down pattern in light REEs (Fig. 7). REE ratios are also similar (e.g., $[La/Sm]_N$ 1.3–1.4$[Sm/Yb]_N$ 2.1–2.5; Fig. 8). All samples show a broad increase in primitive mantle normalized trace element concentrations with increasing incompatibility, save for the most incompatible elements, Rb and Ba, which are depleted relative to more compatible Th and Nb (Fig. 5).

Glass from sample NA064-114 was measured for H_2O, CO_2, Cl, F, and S. The sample has a H_2O concentration of 0.87 wt%, a CO_2 concentration of 135 ppm, Cl concentration of 210 ppm, F concentration of 891 ppm, and S concentration of 1636 ppm (Table 2). All samples have high vesicularities, on the order of 50%, so significant degassing likely occurred prior to eruption.

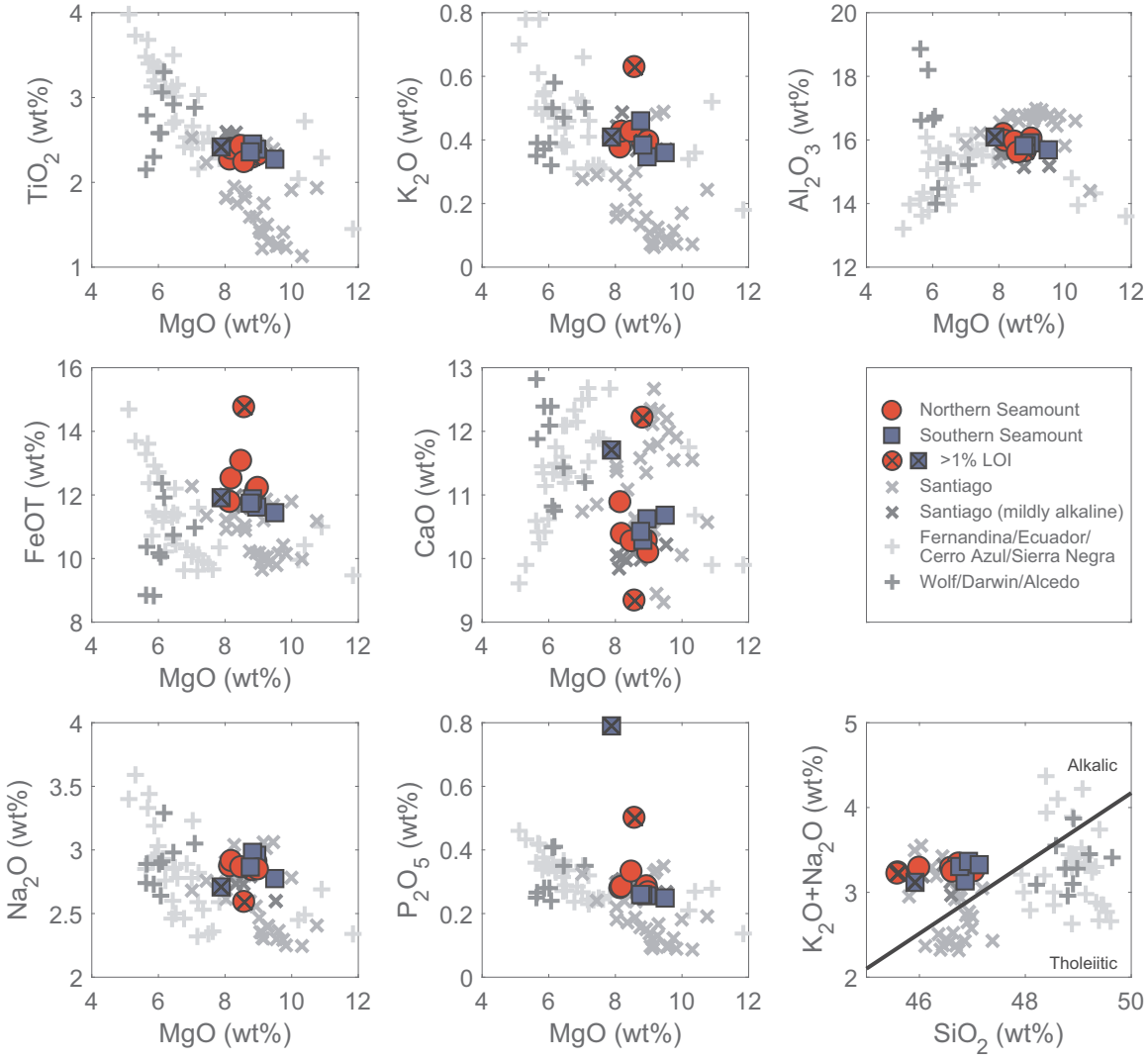

Fig. 3. Major element variations of seamount lavas. Outlined colored markers show data from this study. Samples with loss on ignition (LOI) > 1 wt% are indicated with black "X". Grey markers show representative lavas from nearby Galápagos volcanoes (Fernandina, Ecuador, Cerro Azul, Sierra Negra, Wolf, Darwin, Alcedo; Saal et al., 2007; Santiago; Gibson et al., 2012). Where not visible, dark grey exes indicating the mildly alkaline Santiago compositions are plotted directly beneath seamount data points. (For interpretation of the references to color in this figure legend, the reader is referred to the web version of this article).

5. Petrogenesis

Major element variability and slight negative slopes in incompatible minor elements (TiO_2, K_2O, P_2O_5) with MgO (Fig. 3) suggest all seamount lavas sampled from these seamounts are related through small extents of fractional crystallization. To test this hypothesis and assess the mean depth of crystallization, we modeled fractional crystallization using alphaMELTS (Ghiorso and Sack, 1995; Asimow and Ghiorso, 1998; Smith and Asimow, 2005). Crystallization models were run at 100, 500 and 900 MPa, QFM buffered, log ΔfO_2 offset of −0.83 (average Galápagos basalt; Rilling, 2005), primitive starting composition (taken from Santa Cruz; Wilson, 2013) and water contents of 0.87 wt% (based on volatile contents in quenched glass from sample NA064-114). This water content is near the upper limit for submarine basaltic glasses analyzed in the Galápagos (0.098–1.15 wt% H_2O; Peterson et al., 2013) but is likely a lower bound given the high vesicularities in these samples.

Results of the petrologic models suggest that the range of major element compositions at both seamounts can be explained by < 10% crystallization of olivine + clinopyroxene from a similar parental magma (Fig. 4), and that the majority of lavas are related by ~ 4% fractional crystallization. Notably, sample NA064-115 is offset from many of the crystallization trends (FeO_T, K_2O, and P_2O_5), which likely results from significant alteration (LOI = 2.38%) of the whole rock. The best-fit trends were produced from crystallization at pressures between 500–900 MPa. Crystallization paths between the north and south seamounts are offset in CaO/Al_2O_3 as a function of Mg# (molecular $MgO/(MgO + FeO_T) \times 100$), which may indicate magma storage and crystallization at variable depths prior to eruption or crystallization during ascent (Fig. 4). In either case, these models suggest that the seamount lavas underwent storage and minor crystallization in a deep (17–35 km) magma chamber. This is significantly shallower than the inferred base of the lithosphere in the region (~ 55 km; Villagómez et al., 2007; Gibson et al., 2012), but is deeper than crustal thickness estimates for the central archipelago (~ 16 km; Feighner and Richards, 1994; Toomey et al., 2001). Thus, these depths imply crystallization in the lithospheric mantle.

Lavas from both seamounts show slight variations in trace element concentrations (e.g., 9.38–10.99 ppm La; Fig. 6). These variations can be produced by fluctuations in extents of partial melting (Shaw, 1970), source variation (e.g., Weaver, 1991), or fractional crystallization (Shaw, 1970). Variations in extents of partial melting or mantle sources with different trace element concentrations will result in differences in trace element ratios (e.g., low extents of melting or mixing with an

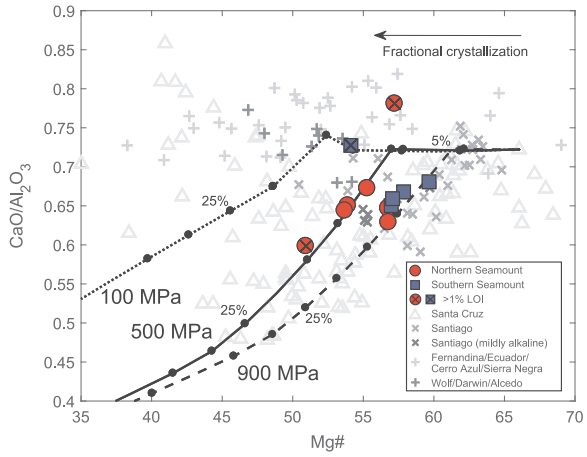

Fig. 4. Variation of CaO/Al_2O_3 as a function of Mg#. Mg# is defined as molecular $MgO/(MgO+FeO_T)*100$. Black lines show isobaric fractional crystallization trends at 100, 500 and 900 MPa, black dots along lines indicate 5% increments of crystal fractionation by mass. Fractional crystallization is modeled from alphaMELTS software (see text for model descriptions). Outlined colored markers show data from this study. Samples with loss on ignition (LOI) > 1 wt% are indicated with black "X". Grey markers show representative lavas from nearby Galápagos volcanoes (Fernandina, Ecuador, Cerro Azul, Sierra Negra, Wolf, Darwin, Alcedo; Saal et al., 2007; Santiago; Gibson et al., 2012; Santa Cruz; Wilson, 2013). (For interpretation of the references to color in this figure legend, the reader is referred to the web version of this article).

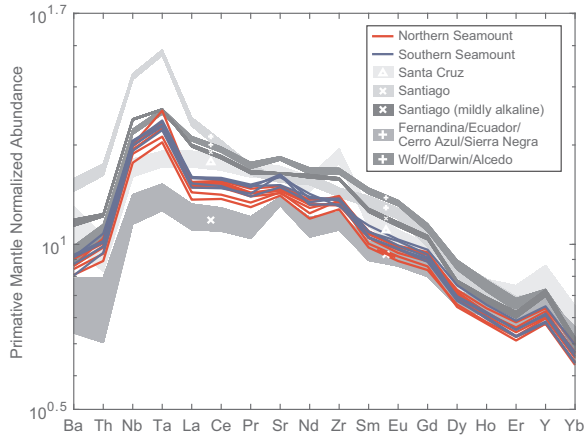

Fig. 5. Trace element diagram comparing the seamount samples to averaged Galápagos Lavas. Elements are listed in order of increasing compatibility and normalized to the primitive mantle (McDonough and Sun, 1995). Colored lines show data from this study. Grey fields show mean value and 2σ range for representative lavas from nearby Galápagos volcanoes (symbols are consistent with previous figures; data sources as indicated in Fig. 4). (For interpretation of the references to color in this figure legend, the reader is referred to the web version of this article).

enriched source will produce high La concentrations and high $[La/Sm]_N$ ratios or low $[La/Nb]_N$ ratios; e.g., Kurz and Geist, 1999). By contrast, limited extents of fractional crystallization, such as those indicated by major element variations (< 10%; Fig. 4) will result in nearly equal enrichments of all incompatible trace elements, preserving trace element ratios. Despite limited variations in trace element concentrations at both seamounts, there are only minor variations in $[La/Sm]_N$ and no variation in $[La/Nb]_N$ (Figs. 6 and 8), indicating that the lavas may be produced by only slight variations in degree of melting of a similar source. The nearly uniform trace element ratios (Figs. 6 and 8) and REE patterns (Fig. 7) are consistent limited fractional crystallization during the evolution of magmas at both seamounts.

White et al. (1993) noted a downstream depletion in highly incompatible trace elements from the center of plume upwelling, attributed to progressive dilution of the mantle plume with entrained upper mantle material. The primitive component of the Galápagos mantle

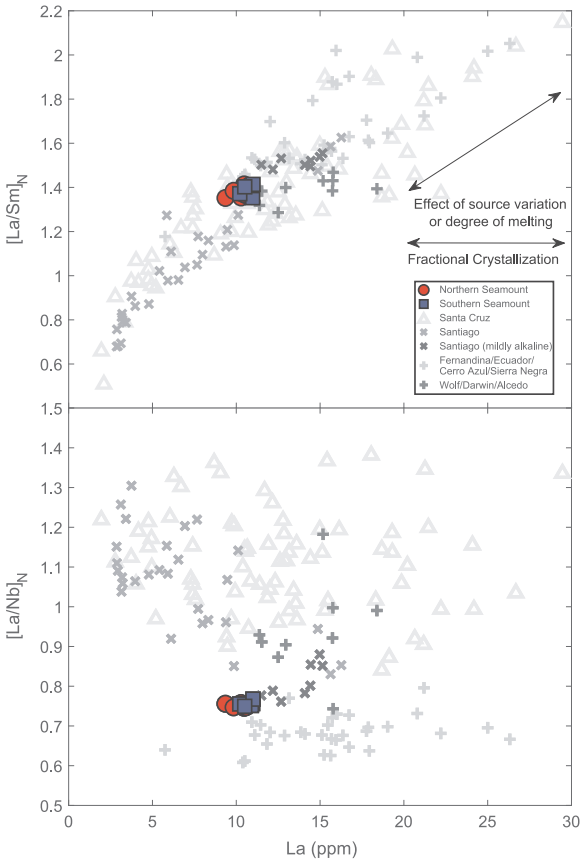

Fig. 6. Variation of $[La/Sm]_N$ and $[La/Nb]_N$ as a function of la concentration. Trace element ratios are normalized to CI (McDonough and Sun, 1995). Outlined colored markers show data from this study. Grey markers show representative lavas from nearby Galápagos volcanoes (data sources as indicated in Fig. 4). (For interpretation of the references to color in this figure legend, the reader is referred to the web version of this article).

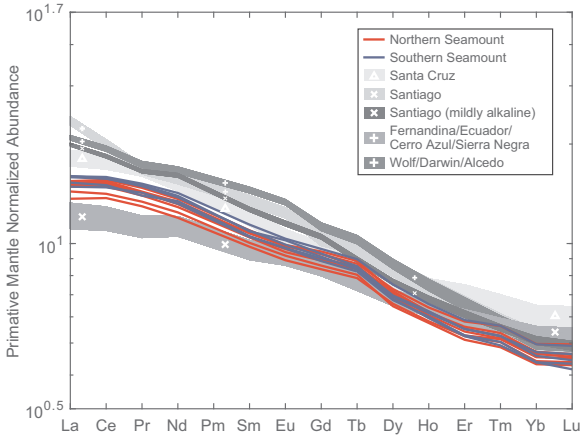

Fig. 7. REE diagram comparing the seamount samples to averaged Galápagos Lavas. Elements are normalized to the primitive mantle (McDonough and Sun, 1995). Colored lines show data from this study. Grey fields show mean value and 2σ range for representative lavas from nearby Galápagos volcanoes (symbols are consistent with previous figures; data sources as indicated in Fig. 4). (For interpretation of the references to color in this figure legend, the reader is referred to the web version of this article).

plume has can be identified by high $^3He/^4He$ isotopic ratios (~ 30 Ra, Kurz and Geist, 1999; Kurz et al., 2009), which correlates with elevated Ti, Ta and Nb, relative to elements of similar compatibilities (Kurz and Geist, 1999; Jackson et al., 2008). This dilution trend is manifested as extremely low $[La/Nb]_N$ ratios in lavas erupted at Fernandina

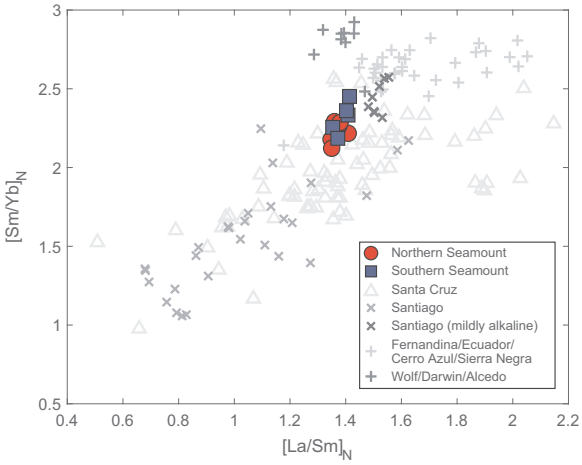

Fig. 8. Variation of $[Sm/Yb]_N$ as a function of $[La/Sm]_N$. Trace element ratios are normalized to CI (McDonough and Sun, 1995). Outlined colored markers show data from this study. Grey markers show representative lavas from nearby Galápagos volcanoes (data sources as indicated in Fig. 4). (For interpretation of the references to color in this figure legend, the reader is referred to the web version of this article).

compared to nearby Wolf, Darwin and Alcedo volcanoes on Isabela Island (Fig. 6; mean $[La/Nb]_N$ 0.67 and 0.97, respectively), despite similar degrees of melting predicted for this region (Gibson and Geist, 2010). The downstream change in these ratios allows us to assess the lateral position of melt generation that produced the seamounts relative to the plume center. Seamount lavas have mean $[La/Nb]_N$ 0.75 (Fig. 6), which is higher than that of lavas erupted at Fernandina. This suggests that the seamounts did not form over the plume center and migrate eastward with plate motion, but instead erupted relatively recently downstream of the plume center.

The dissolved CO_2 concentration measured in sample NA064-114 (135 ppm) is ~ 95% less than presumably undegassed Galápagos melt inclusion contents (up to 5821 ppm CO_2; Koleszar et al., 2009). This concentration is also much lower than the range of CO_2 (4200–5600 ppm) predicted from CO_2/Nb for undegassed mid-ocean ridge basalts (300; Saal et al., 2002) and Gálapagos lavas (400; Peterson et al., 2013) using mean Nb values of the seamount samples (14 ppm). By contrast, S (1636 ppm) is comparable to that of S measured in undersaturated submarine glasses collected at greater water depths (1599 ppm; Peterson et al., 2010). Despite evidence for extensive degassing (high vesicularites), the CO_2 contents are still greater than predicted for their eruption depths. Any excess volatile concentrations, relative to experimentally derived solubility curves, likely result from rapid ascent and quenching with insufficient time for degassing (e.g., Dixon et al., 1988; le Roux et al., 2006). We use the dissolved CO_2 and H_2O concentrations measured in NA064-114 (135 ppm and 0.87 wt%, respectively) to yield a vapor saturation pressure of 36 MPa, which is equivalent to ~ 1.2 km below seafloor (Dixon and Stolper, 1995; Newman and Lowenstern, 2002). Thus, we suggest that the exsolution of CO_2 and H_2O, within a magmatic system at > 1.2 km depth drove rapid magma ascent, vesiculation and fragmentation. Fragmentation may also be enhanced by seawater interaction, common for submarine volcanoes at depths between 200 and 1300 m (Allen and McPhie, 2009). This is consistent with pyroclastic activity forming a majority of the volume of each seamount edifice, followed by limited extents of effusive volcanism associated with crater filling pillow lava and flows.

The similarity between the two seamounts in major elements (Fig. 3), trace element contents (Fig. 5) and ratios (Figs. 6 and 8) indicates that they were either produced from the same mantle source and evolved under similar conditions or shared the same batch of magma and were erupted over a short duration. Similarity in morphological features between the two seamounts, including outer slope angles and southwestward breaching, indicates similarity in vent conditions and ocean currents during eruption (e.g., Settle, 1979). Combined with the spatial proximity of the two seamounts, we suggest that, together, the seamounts were produced during a single eruptive event or closely timed events originating from the same magma batch. Individual seamount volumes (0.14–0.36 km^3) are on the order of other single lava flows observed in the Galápagos (0.12 km^3; Rowland, 1996), and combined are less than the total volume for single eruptive events described for multiple events at Fernandina (2 km^3; Simkin and Howard, 1970; 2.3 km^3; Rowland, 1996), thus it is conceivable that both were produced from a single monogenic basaltic eruption.

6. Comparison of seamounts to the western and eastern volcanic systems on the Galápagos Platform

6.1. Extents of melting and lithospheric thickness

The mean extent of melting experienced by the upwelling mantle beneath a hotspot volcano is controlled by the depth difference between the solidus and the base of the lithosphere (e.g., McKenzie and Bickle, 1988). In the Galápagos, there is a change in lithospheric thickness from 70 km in the west to 40 km in the east (Villagómez et al., 2007). As a result, western volcanoes undergo lower mean extents of melting than those in the east (Gibson and Geist, 2010), despite a deeper onset of melting resulting from higher excess temperatures (Villagómez et al., 2007) and chemical enrichment (White et al., 1993). Mean extents of melting for magmas of a similar source composition can be assessed from the ratios of REEs or slopes in primitive mantle normalized REE diagrams (e.g., Gibson and Geist, 2010). At low extents of melting, light REEs will be fractionated into the melt to greater extents than heavy REEs, creating relatively steep patterns and elevated trace element ratios. The depth to the top of the melting column (serving as a proxy for mean extent of melting) can be calculated from empirical relationships between both $[La/Sm]_N$ and $[Sm/Yb]_N$, which are derived from REE inversion modeling (Eqs. (1), (2) in Gibson and Geist (2010)).

Determining relative extents of melting across the Galápagos is complicated by mantle source heterogeneities, which also vary from west to east across the archipelago (e.g., White et al., 1993). Lower negative slopes in REEs are predicted with increasing distance from the plume due to decreasing extent of "plume" material in the source (White et al., 1993). Fortunately, the degree of source enrichment can be evaluated independently of melting processes through the use of radiogenic isotopes (e.g., Gibson et al., 2012). While we have not measured radiogenic isotope ratios in the seamount lavas, there is little variation in $^{87}Sr/^{86}Sr$ and $^{206}Pb/^{207}Pb$ in lavas with $[La/Nb]_N < 0.9$ from volcanoes adjacent to the seamounts (Wolf and Darwin; Western Santiago), suggesting similar mantle sources (Gibson et al., 2012). Seamount lavas have $[La/Nb]_N$ ranging from 0.74 to 0.77, thus we assume a similar source composition between seamounts and lavas erupted at nearby islands. Additionally, to minimize the impact of this assumption, we choose to only evaluate depth to the top of the melting column using $[Sm/Yb]_N$, which is less sensitive to source variation than $[La/Sm]_N$ (Gibson and Geist, 2010).

The mean REE slope of the western volcanoes is greater than that of the eastern volcanoes, suggesting lower mean extents of melting, and consistent with a thicker lithosphere (Fig. 7). The nearest western volcanoes to the seamounts (Wolf, Darwin and Alcedo on Isabela Island) have mean $[Sm/Yb]_N$ of 2.55, attributed to a depth to the top of the melting column at 57 km (Gibson and Geist, 2010). By comparison, eastern volcanoes (Santiago and Santa Cruz Islands) have lower mean $[Sm/Yb]_N$ of 1.55, which equates to a shallower depth to the top of the melting column of 53 km. Notably however, there is a break in $[Sm/Yb]_N$ from W-E across the island of Santiago (56 km vs. 53 km, respectively; Gibson et al., 2012) suggesting that the transition between thick and thin lithosphere is relatively sharp and dissects the island into a western and eastern volcanic system, assuming melts ascend vertically from their source. The seamount REE patterns (Fig. 7) and ratios

(Fig. 8) are intermediate between western and eastern volcanoes, suggesting that magmas producing the seamounts were generated from intermediate mean extents of melting. Seamount lavas have an average $[Sm/Yb]_N$ of 2.3 (Fig. 8), corresponding to a depth to the top of the melting column of 56 km (Eq. (1) in Gibson and Geist (2010)). This depth falls between that of the western and eastern volcanoes on average, but is more consistent with the thicker lithosphere of the western volcanoes and is identical to that of western Santiago.

6.2. Crystallization and melt storage

The seamounts are located within a major transition in volcano morphology and magma storage depth between the western and eastern volcanic provinces on the Gálapagos Platform. Lavas erupted at western Galápagos volcanoes are produced by relatively high extents of fractional crystallization (average MgO of 6.79 wt%; e.g., Saal et al., 2007) in shallow crustal magma chambers (~ 200 MPa; Geist et al., 1998). By contrast, lavas erupted at eastern volcanoes undergo less fractional crystallization (average of 8.34 wt% MgO; Gibson et al., 2012; Wilson, 2013) at greater depths (~ 600 MPa; Geist et al., 1998).

All of the seamount lavas are relatively mafic, with MgO contents > 7.7 wt%, suggesting limited crystallization prior to eruption. These MgO contents are higher than the narrow range that is typically observed on the western islands of Fernandina and Isabela (Fig. 3; e.g., Saal et al., 2007), but fall within the range of the eastern volcanoes (Fig. 3; e.g., Gibson et al., 2012; Wilson, 2013). Petrologic modeling indicates that crystallization depths of ~ 17–30 km (equivalent to 500–900 MPa; Fig. 4), consistent with deeper magmatic plumbing systems at eastern volcanoes of ~ 21 km (Santa Cruz, Santiago, San Cristobal; 600 ± 100 MPa; Geist et al., 1998). Thus trace element patterns and ratios of the seamount lavas share melting characteristics similar to western Santiago and Wolf, Darwin and Alcedo volcanoes on Isabela, while the magma storage conditions closely resemble those associated with the eastern volcanoes.

7. Shared seamount magma plumbing with Santiago?

The closest island to the two seamounts is Santiago (Fig. 2), which is 5 km to the northeast, near the northern edge of the Galápagos Platform (Fig. 1). The island has morphological characteristics of the eastern volcanoes, lacking a large central caldera and having lower eruption rates compared to the more active western volcanoes (Fig. 1; Geist et al., 2008b). Santiago remains volcanically active, with historical eruptions occurring on the eastern side of the island in 1906 and on the western side in ~ 1754 (Siebert et al., 2011). Lavas erupted on Santiago are highly variable, with rock types ranging from picrites to trachytes (McBirney and Williams, 1969; Saal et al., 2007; Herbert et al., 2009; Gibson et al., 2012). Geochemical analyses of subaerial basalts indicate variable major and trace element compositions (tholeiitic, transitional, and alkalic) that are spatially distributed across the island (Gibson et al., 2012). The western portion of the island is dominated by eruption of mildly alkaline basalts, while the eastern portion of the island has erupted both tholeiitic and transitional basalts. This compositional zonation from west to east is thought to occur due to an abrupt change in the lithospheric thickness directly below Santiago (Gibson et al., 2012).

Trace element patterns in mildly alkaline lavas on western Santiago are interpreted to result from melting directly beneath that side of the island, where thicker lithosphere truncates the melting column at greater depths (Gibson et al., 2012). The seamount lavas are compositionally similar to the mildly alkaline series and in particular, a subset of lavas erupted subaerially on the western flank of Santiago (hereon referred to as the Western Mildly Alkaline (WMA) lavas; Gibson et al., 2012). WMA lavas are distinguished from other mildly alkalic lavas on the western side of the island by low $[La/Ba]_N$ ratios and similar trace element patterns. Both the seamounts and WMA lavas have undergone similar degrees of crystallization (means of 8.68 and 8.79 wt% MgO, respectively) at similar storage depths of 17–35 km (interpreted from similar mean CaO/Al_2O_3 of 0.67 and 0.65, respectively). Moreover, similar mantle source and degrees of melting are inferred for seamount and WMA lavas based on REE abundances (10 and 11 mean ppm La, respectively) and mean $[La/Sm]_N$ ratios (1.38 and 1.51, respectively). Similar depths to the top of the melting column are inferred from mean $[Sm/Yb]_N$ (2.26 and 2.35 respectively). The similarities between seamounts and WMA lavas are even recognizable in the most nuanced variations in trace elements, including negative Ba anomaly and slightly positive Sr and Zr anomalies (Fig. 9).

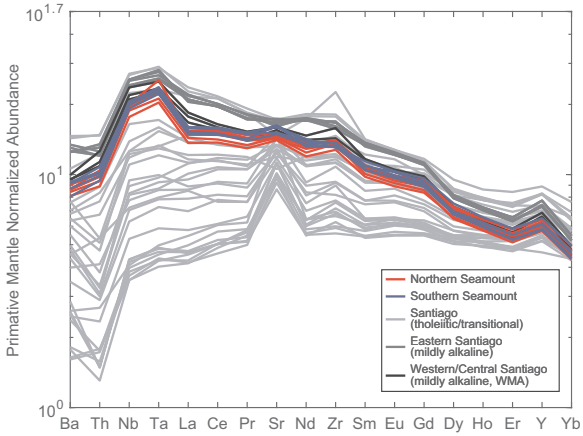

Fig. 9. Trace element diagram comparing the seamount samples to Santiago Lavas. Elements are listed in order of relative compatibility and normalized to the primitive mantle (McDonough and Sun, 1995). Colored lines show data from this study. Grey lines show Santiago lava compositions simplified from Gibson et al. (2012). (For interpretation of the references to color in this figure legend, the reader is referred to the web version of this article).

Based on these geochemical similarities, the seamount and WMA lavas are either produced from a single magmatic event or two separate events, under nearly identical conditions. If the seamounts were produced in a separate magmatic event, their chemical similarities, outlined above, would require that they underwent the same degree of melting of the same source, with similar transport and crystallization histories as the WMA lavas. We assert that it is much simpler to assume that lavas for both seamounts were produced in a single batch, and passed through the same magma plumbing system. Thus, we conclude that the seamount and WMA lavas are sourced from the same central reservoir in the lithospheric mantle (500–900 MPa; Fig. 10) beneath Santiago and erupted over a relatively short time period. The distribution of WMA and seamount lavas implies that, in the absence of shallow magma reservoirs in the eastern archipelago, magmas stored deep in the crust can be transported laterally on the order of 10 km in subsurface dikes prior to eruption (Fig. 10). We propose that lateral magma migration begins between the transition into the elastic crust at 6–12 km (Feighner and Richards, 1994) and depths derived from CO_2 and H_2O vapor saturation pressures at 1.2 km (Section 5; Fig. 10). In Hawaii, similar dike dimensions (15–25 km lateral extent by 4–8 km vertical extent) have been inferred from limits of seismic swarms during emplacement events (Rubin and Pollard, 1988). This finding differs from that of Gibson et al. (2012), who, based on the geochemistry of the subaerial sample suite suggest that there is limited lateral transport of magmas during ascent through the lithosphere. This highlights the importance of investigating submarine features around the main islands on the platform in order to better understand the complexities of melt generation and construction of the archipelago.

Given the transitional nature and compositional similarity of the lavas from the two seamounts and WMA lavas, in both maximum depths and extents of melting, we prefer a model where melts may be generated in the mantle over a wide region between Alcedo and Santiago (~ 50 km wide; Fig. 10), but are channeled through and

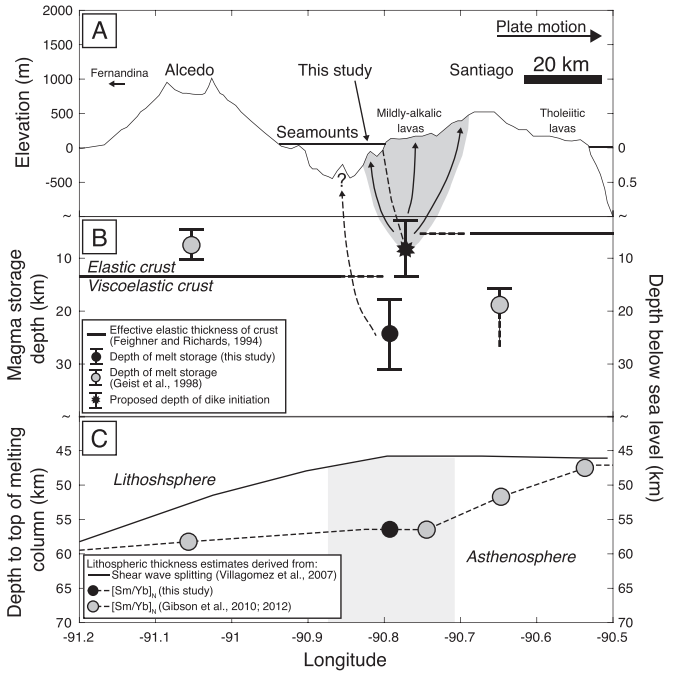

Fig. 10. Schematic cross-section depicting seamount genesis. A) Thin black line is an elevation profile from W-E across the Galápagos Platform, from Alcedo Volcano on Isabela Island to Santiago Island. Thick black horizontal line shows sea level. Dark grey region is the proposed extent of shallow diking, resulting in distribution of mildly alkalic lavas from seamounts to central Santiago. Dashed line within the diking region indicates a separation between the seamount lavas from those erupted subaerially. Solid arrows indicate rapid melt transport in elastic crust evidenced by limited shallow degassing of lavas (Section 5). Dashed arrow shows potential melt transport pathway for other unexplored seamounts. B) Solid line is the effective elastic thickness of crust (Feighner and Richards, 1994). Black circle indicates range of melt storage and crystallization depths for seamount lavas, derived from CaO/Al_2O_3 ratios (Section 5). Grey circles indicate range of melt storage depths for Alcedo and Santiago (Geist et al., 1998). Black decagram indicates depth of dike initiation constrained by transition into the elastic crust (6–12 km) and depths derived from CO_2 and H_2O vapor saturation pressures (1.2 km; Section 5). C) Solid black line indicates lithospheric thickness derived from shear wave splitting data (Villagómez et al., 2007). Black circle indicates top of the melting column calculated from average $[Sm/Yb]_N$ values of seamount samples from this study. Grey circles indicate top of the melting column calculated from average $[Sm/Yb]_N$ values from Alcedo (Gibson and Geist, 2010) and Santiago (Gibson et al., 2012). Black dashed line is the lithospheric thickness derived from the combined $[Sm/Yb]_N$ calculations. Light grey region indicates the potential melting region for seamount lavas.

homogenized within the deep magmatic system associated with western Santiago prior to their redistribution in the shallow crust. In this case, even if mantle heterogeneity or lithospheric thickness undergo gradual changes across the archipelago, the variations are discretized in the nearest island's complex plumbing system. Further geochemical and morphological investigations of seamounts throughout the Galápagos Platform, and comparisons to nearby volcanoes would help determine the extent to which the major volcano magmatic systems control the geochemistry of intra-island seamounts.

8. Conclusion

Similarities in major and trace element concentrations and ratios suggest that lavas erupted from two seamounts between the islands of Isabela and Santiago in the Galápagos Archipelago are from the same parental magma. The seamounts were likely produced by rapid magma ascent from depths > 1.2 km, resulting in the construction of the main edifices by both explosive and effusive volcanism. Magma supplied to the seamounts were generated away from the plume center and underwent storage and minor crystallization in a chamber located in the lithospheric mantle (17–35 km; Figs. 4 and 10).

Total extents of melting, as indicated by intermediate average REE patterns, and $[Sm/Yb]_N$ are transitional between the western and eastern regions of the archipelago (Figs. 7 and 8; Gibson and Geist, 2010), and closely resemble those of the nearby western volcanoes of Wolf, Darwin and Alcedo on Isabela Island, as well as western Santiago, in average trace element contents (Fig. 5). These data suggest that seamount magmas were generated above a lithosphere of intermediate thickness similar conditions beneath eastern Isabela and western Santiago. Despite this, seamount magmas appear to have a transport and storage history more akin to that of the eastern volcanoes (e.g., low extents of fractional crystallization, Fig. 3; deep storage, Fig. 4), reflecting lower magma supply and deeper crystallization. These compositional characteristics signify that, although seamount magmas have a transitional melting signature, their crustal signature suggests they are parasitic to Santiago and pass through a shared plumbing system that has also erupted subaerial lavas (Fig. 10).

Given the transitional nature of the seamount lavas, in both maximum depths and extents of melting, between that of the western and eastern volcanoes, we prefer a model where melts are generated over a ~ 50 km wide region beneath the seamounts and the island, but are homogenized in the lithospheric mantle and are channeled through western Santiago's crustal plumbing system and transported laterally on the order of 10 km in subsurface dikes prior to eruption on the shallow submarine platform (Fig. 10). The Galápagos Platform is studded with numerous clusters and lineaments of small seamounts adjacent to the islands, most of which have never been sampled. Further detailed geological and geochemical investigations of these seamounts and their relationship to adjacent volcanoes would enable a better assessment of the extent of magma partitioning between subaerial and submarine systems' relationship to seamount and subaerial morphologies as well as the origins of the magmas in both settings.

Acknowledgements

We thank the Ocean Exploration Trust, and the crew of the E/V *Nautilus* for facilitating the mapping and sample collection for this project. Thank you to the NOAA Office of Exploration and Research for funding the E/V *Nautilus* Exploration Program (NA15OAR0110220). Additionally, we are grateful to the Galápagos National Park directorate for allowing the collection of submarine rock samples through joint permit (PC-45-15) in collaboration with the Charles Darwin Research Foundation. We also gratefully recognize the Government of Ecuador via the Ecuadorian Navy for permission to operate in their territorial waters and marine protected areas. We appreciate the WSU Geoanalytical Facility and WHOI Ionprobe Facility for XRF and volatile analysis, respectively. Work for this project was carried out with support provided by the NSF (OCE-1634952 to VDW, OCE-1634685 to SAS) and the Dalio Explore Fund and Investment in Science Fund at WHOI. We also thank Bill Chadwick and an anonymous reviewer for their comments and suggestions, which greatly improved the final manuscript.

Appendix A. Supplementary material

Supplementary data associated with this article can be found in the online version at http://dx.doi.org/10.1016/j.dsr2.2017.09.019.

References

Allan, J.F., Simkin, T., 2000. Fernandina Volcano's evolved, well-mixed basalts: mineralogical and petrological constraints on the nature of the Galápagos plume. J. Geophys. Res. 105, 6017. http://dx.doi.org/10.1029/1999JB900417.

Allen, S.R., McPhie, J., 2009. Products of neptunian eruptions. Geology 37, 639–642.

Asimow, P.D., Ghiorso, M.S., 1998. Algorithmic modifications extending MELTS to calculate subsolidus phase relations. Am. Mineral. 83, 1127–1132.

Bell, K.L.C., Brennan, M.L., Flanders, J., Raineault, N.A., Wagner, K., 2016. New Frontiers in Ocean Exploration: The E/V Nautilus and NOAA Ship Okeanos Explorer, 2015 Field Season.

Carey, B.S., Fisher, C.R., Leon, P.S. De, Roman, C., Raineault, N.A., Suarez, J., Smart, C.,

Kane, R., Tüzün, S., Balcanoff, J., Lubetkin, M., Jones, M., Schwartz, D., Fornari, D., Soule, A., Wanless, D., Watling, L., Ballard, R.D., 2016. Exploring the Undersea World of the Galápagos Islands Exploring the Undersea World of the Galápagos Islands.
Chadwick, W.W., Dieterich, J.H., 1995. Mechanical modeling of circumferential and radial dike intrusion on Galápagos volcanoes. J. Volcanol. Geotherm. Res. 66, 37–52.
Chadwick, W.W., Howard, K.A., 1991. The pattern of circumferential and radial eruptive fissures on the volcanoes of Fernandina and Isabela islands, Galápagos. Bull. Volcanol. 53, 259–275. http://dx.doi.org/10.1007/BF00414523.
Christie, D.M., Duncan, R.A., McBirney, A.R., Richards, M.A., White, W.M., Harpp, K.S., Fox, C.G., 1992. Drowned islands downstream from the Galápagos hotspot imply extended speciation times. Nature 355, 246–248. http://dx.doi.org/10.1038/355246a0.
Clague, D.A., Dalrymple, G.B., 1987. The Hawaiian-emperor volcanic chain. Part I. Geologic evolution. Volcanism Hawaii 1, 5–54.
Dixon, J.E., Stolper, E.M., 1995. An experimental study of water and carbon dioxide solubilities in mid-ocean ridge basaltic liquids. Part II: applications to degassing. J. Petrol. 36, 1633–1646.
Dixon, J.E., Stolper, E.M., Delaney, J.R., 1988. Infrared spectroscopic measurements of CO_2 and H2O in Juan de Fuca Ridge basaltic glasses. Earth Planet. Sci. Lett. 90, 87–104. http://dx.doi.org/10.1016/0012-821X(88)90114-8.
Feighner, M.A., Richards, M.A., 1994. Lithospheric structure and compensation mechanisms of the Galápagos Archipelago. J. Geophys. Res. 99, 6711–6729.
Geist, D., 1996. On the emergence and submergence of the Galápagos Islands. Not. Galápagos 56, 5–9.
Geist, D., Harpp, K., 2009. Galápagos Islands: Geology. Encycl. Islands.
Geist, D., Naumann, T., Larson, P., 1998. Evolution of Galápagos magmas: mantle and crustal fractionation without assimilation. J. Petrol. 39, 953–971.
Geist, D., Diefenbach, B.A., Fornari, D.J., Kurz, M.D., Harpp, K., Blusztajn, J., 2008a. Construction of the Galápagos platform by large submarine volcanic terraces. Geochemistry. Geophys. Geosyst. 9. http://dx.doi.org/10.1029/2007GC001795.
Geist, D., Snell, H., Snell, H., Goddard, C., Kurz, M.D., 2014a. A paleogeographic model of the Galápagos Islands and biogeographical and evolutionary implications. In: Harpp, Karen S., Mittelstaedt, Eric, d'Ozouville, Noémi, Graham, D.W. (Eds.), The Galápagos: A Natural Laboratory for the Earth Sciences, Geophysical Monograph 204. John Wiley & Sons, Inc, pp. 145–166.
Geist, D.J., McBirney, A.R., Duncan, R.A., 1986. Geology and petrogenesis of lavas from San Cristobal Island, Galapagos Archipelago. Geol. Soc. Am. Bull. 97, 555. http://dx.doi.org/10.1130/0016-7606(1986)97<555:GAPOLF>2.0.CO;2.
Geist, D.J., Harpp, K.S., Naumann, T.R., Poland, M., Chadwick, W.W., Hall, M., Rader, E., 2008b. The 2005 eruption of Sierra Negra volcano, Galápagos, Ecuador. Bull. Volcanol. 70, 655–673. http://dx.doi.org/10.1007/s00445-007-0160-3.
Geist, D.J., Bergantz, G., Chadwick, W.W., 2014b. Galápagos magma chambers. In: Harpp, Karen S., Mittelstaedt, Eric, d'Ozouville, Noémi, Graham, D.W. (Eds.), The Galápagos: A Natural Laboratory for the Earth Sciences, Geophysical Monograph 204. John Wiley & Sons, Inc, Washington, DC, pp. 55–70.
Ghiorso, M.S., Sack, R.O., 1995. Chemical mass transfer in magmatic processes IV. A revised and internally consistent thermodynamic model for the interpolation and extrapolation of liquid-solid equilibria in magmatic systems at elevated temperatures and pressures. Contrib. Mineral. Petrol. 119, 197–212.
Gibson, S., Geist, D., 2010. Geochemical and geophysical estimates of lithospheric thickness variation beneath Galápagos. Earth Planet. Sci. Lett. 300, 275–286. http://dx.doi.org/10.1016/j.epsl.2010.10.002.
Gibson, S., Geist, D.J., Day, J., Dale, C.W., 2012. Short wavelength heterogeneity in the Galápagos plume: evidence from compositionally diverse basalts on Isla Santiago. Geochem. Geophys. Geosyst. 13, Q09007. http://dx.doi.org/10.1029/2012GC004244.
Goss, A.R., Perfit, M.R., Ridley, W.I., Rubin, K.H., Kamenov, G.D., Soule, S.A., Fundis, A., Fornari, D.J., 2010. Geochemistry of lavas from the 2005–2006 eruption at the East Pacific Rise, 9°46′N-9°56N: implications for ridge crest plumbing and decadal changes in magma chamber compositions. Geochem., Geophys. Geosyst. 11, 1–35. http://dx.doi.org/10.1029/2009GC002977.
Harpp, K., Geist, D., 2002. Wolf–Darwin lineament and plume–ridge interaction in northern Galápagos. Geochem. Geophys. Geosyst. 3, 1–19.
Harpp, K.S., Fornari, D.J., Geist, D.J., Kurz, M.D., 2003. Genovesa submarine Ridge: a manifestation of plume-ridge interaction in the northern Galápagos Islands. Geochem. Geophys. Geosyst. 4.
Hauri, E., Wang, J., Dixon, J.E., King, P.L., Mandeville, C., Newman, S., 2002. SIMS analysis of volatiles in silicate glasses 1. Calibration, matrix effects and comparisons with FTIR. Chem. Geol. 183, 99–114. http://dx.doi.org/10.1016/S0009-2541(01)00375-8.
Herbert, S., Gibson, S., Norman, D., Geist, D.J., Estes, G., Grant, T., Miles, A., 2009. Into the field again: re-examining Charles Darwin's 1835 geological work on Isla Santiago (James Island) in the Galápagos Archipelago. Earth Sci. Hist.
Hooft, E.E.E., Toomey, D.R., Solomon, S.C., 2003. Anomalously thin transition zone beneath the Galápagos hotspot. Earth Planet. Sci. Lett. 216, 55–64.
Jackson, M.G., Hart, S.R., Saal, A.E., Shimizu, N., Kurz, M.D., Blusztajn, J.S., Skovgaard, A.C., 2008. Globally elevated titanium, tantalum, and niobium (TITAN) in ocean island basalts with high 3He/4He. Geochem. Geophys. Geosyst. 9. http://dx.doi.org/10.1029/2007GC001876.
Johnson, D.M., Hooper, P.R., Conrey, R.M., 1999. XRF analysis of rocks and minerals for major and trace elements on a single low dilution Li-tetraborate fused bead. Adv. X-ray Anal. 41, 843–867.
Kelley, K.A., Plank, T., Ludden, J., Staudigel, H., 2003. Composition of altered oceanic crust at ODP Sites 801 and 1149. Geochem. Geophys. Geosyst. 4.
Koleszar, A.M., Saal, A.E., Hauri, E.H., Nagle, A.N., Liang, Y., Kurz, M.D., 2009. The volatile contents of the Galápagos plume; evidence for H2O and F open system behavior in melt inclusions. Earth Planet. Sci. Lett. 287, 442–452.
Kurz, M., Geist, D., 1999. Dynamics of the Galápagos hotspot from helium isotope geochemistry. Geochim. Cosmochim. Acta 63, 4139–4156.
Kurz, M.D., Curtice, J., Fornari, D., Geist, D., Moreira, M., 2009. Primitive neon from the center of the Galápagos hotspot. Earth Planet. Sci. Lett. 286, 23–34. http://dx.doi.org/10.1016/j.epsl.2009.06.008.
Lytle, M.L., Kelley, K.A., Hauri, E.H., Gill, J.B., Papia, D., Arculus, R.J., 2012. Tracing mantle sources and Samoan influence in the northwestern Lau back-arc basin. Geochem. Geophys. Geosyst. 13.
McBirney, A.R., Williams, H., 1969. Geology and petrology of the Galápagos Islands. Geol. Soc. Am. Mem. 118, 1–197.
McDonough, W.F., Sun, S.S., 1995. The composition of the Earth. Chem. Geol. 120, 223–253.
McKenzie, D., Bickle, M.J., 1988. The volume and composition of melt generated by extension of the lithosphere. J. Petrol. 29, 625–679.
Morgan, W.J., 1972. Deep mantle convection plumes and plate motions. Am. Assoc. Pet. Geol. Bull. 56, 203–213.
Newman, S., Lowenstern, J.B., 2002. VolatileCalc: a silicate melt–H2O–CO2 solution model written in Visual Basic for Excel. Comput. Geosci. 28, 597–604.
Peterson, M., Saal, A.E., Hauri, E.H., Werner, R., Hauff, S.F., Kurz, M.D., Geist, D., Harpp, K.S., 2010. Sources of volatiles in basalts from the Galápagos Archipelago: deep and shallow evidence. In: Proceedings of the AGU Fall Meeting Abstracts.
Peterson, M., Saal, A., Hauri, E., Kurz, M., Werner, R., Hauff, F., Geist, D., Harpp, K., 2013. Volatile budget of the Galápagos Plume. In: Proceedings of the Goldschmidt 2013 Conference Abstract 1956.
Rilling, S.E., 2005. Oxygen fugacities of lavas from the Galápagos islands and the Galápagos spreading center. In: Proceedings of the AGU Fall Meeting Abstracts.
le Roux, P.J., Shirey, S.B., Hauri, E.H., Perfit, M.R., Bender, J.F., 2006. The effects of variable sources, processes and contaminants on the composition of northern EPR MORB (8–10 N and 12–14 N): Evidence from volatiles (H2O, CO2, S) and halogens (F, Cl). Earth Planet. Sci. Lett. 251, 209–231.
Rowland, S.K., 1996. Slopes, lava flow volumes, and vent distributions on Volcan Fernandina, Galápagos Islands. J. Geophys. Res. Solid Earth 101, 27657–27672.
Rubin, A.M., Pollard, D.D., 1988. Dike-induced faulting in rift zones of Iceland and Afar. Geology 16, 413–417.
Saal, A.E., Hauri, E.H., Langmuir, C.H., Perfit, M.R., 2002. Vapour Undersaturation in Primitive Mid-ocean-ridge Basalt and the Volatile Content of Earth's Upper Mantle. 41.
Saal, A.E., Kurz, M.D., Hart, S.R., Blusztajn, J.S., Blichert-Toft, J., Liang, Y., Geist, D.J., 2007. The role of lithospheric gabbros on the composition of Galápagos lavas. Earth Planet. Sci. Lett. 257, 391–406.
Settle, M., 1979. The structure and emplacement of cinder cone fields. Am. J. Sci. 279, 1089–1107.
Shaw, D.M., 1970. Trace element fractionation during anatexis. Geochim. Cosmochim. Acta 34, 237–243.
Siebert, L., Simkin, T., Kimberly, P., 2011. Volcanoes of the World. Univ of California Press, Berkeley; Los Angeles; London.
Simkin, T., Howard, K.A., 1970. Caldera collapse in the Galápagos Islands, 1968. Science (80) 169, 429–437.
Smith, P.M., Asimow, P.D., 2005. Adiabat_1ph: a new public front-end to the MELTS, pMELTS, and pHMELTS models. Geochem. Geophys. Geosyst. 6.
Swanson, F.J., Baitis, H.W., Lexa, J., Dymond, J., 1974. Geology of Santiago, Rábida, and Pinzón Islands, Galápagos. Geol. Soc. Am. Bull. 85, 1803–1810.
Toomey, D.R., Hooft Toomey, E.E., Hooft Toomey, E.E., Detrick, R.S., 2001. Crustal thickness variations and internal structure of the Galápagos Archipelago In: Proceedings of the AGU Fall Meeting Abstracts.
Villagómez, D.R., Toomey, D.R., Hooft, E.E.E., Solomon, S.C., 2007. Upper mantle structure beneath the Galápagos Archipelago from surface wave tomography. J. Geophys. Res. 112, B07303. http://dx.doi.org/10.1029/2006JB004672.
Villagómez, D.R., Toomey, D.R., Hooft, E.E.E., Solomon, S.C., 2011. Crustal structure beneath the Galpagos Archipelago from ambient noise tomography and its implications for plume-lithosphere interactions. J. Geophys. Res. Solid Earth 116, 1–20. http://dx.doi.org/10.1029/2010JB007764.
Weaver, B.L., 1991. The origin of ocean island basalt end-member compositions: trace element and isotopic constraints. Earth Planet. Sci. Lett. 104, 381–397.
White, W.M., McBirney, A.R., Duncan, R.A., 1993. Petrology and geochemistry of the Galápagos Islands: portrait of a pathological mantle plume. J. Geophys. Res. Solid Earth 98, 19533–19563.
Wilson, E.L., 2013. The Geochemical Evolution of Santa Cruz Island, Galápagos Archipelago. University of Idaho, Moscow (ID).
Yun, S., Segall, P., Zebker, H., 2006. Constraints on magma chamber geometry at Sierra Negra Volcano, Galápagos Islands, based on InSAR observations. J. Volcanol. Geotherm. Res. 150, 232–243. http://dx.doi.org/10.1016/j.jvolgeores.2005.07.009.